Stud. Univ. Babeş-Bolyai Math. 67(2022), No. 4, 891–903
DOI: 10.24193/subbmath.2022.4.16

Mathematical modelling of free convection in a square cavity filled with a bidisperse porous medium for large values of Rayleigh number

Cornelia Revnic and Flavius Pătrulescu

Abstract. A free convection problem for bidisperse porous media is considered. The numerical solutions are obtained using an algorithm based on an nonuniform grid. Results for some values of the governing parameters when Rayleigh number is equal to 10^4 are provided.

Mathematics Subject Classification (2010): 76R10, 76S05, 76M20, 65N06.

Keywords: Numerical results, free convection, square cavity, bidisperse porous medium, nonuniform grid.

1. Introduction

Fluid flow and heat transfer in porous media represented the subject of intensive research in the last decades. A comprehensive presentation of the volume of work in this domain can be found in [14]. In the past several years, there has been much interest in double porosity materials, the so called bidisperse porous media (BDPM). The literature in the field is extensive, see for instance [20] and references therein. A very good description of the mathematical models concerning heat transfer and fluid flow in BDPM can be found in the excellent chapter [15] in the book [10].

A new mathematical model which describes the flow and heat transfer in a square cavity filled with BDPM was considered in [18]. It represents an extension of the classical problem of steady Darcy free convection for a monodisperse (regular) porous medium by following the model proposed in [16] and [17]. The basic equations were transformed in terms of dimensionless stream functions and temperatures and an algorithm based on finite difference method was provided to obtain the numerical solutions.

Received 08 September 2020; Accepted 14 December 2020.

The current paper represents a continuation of [18] and we use a different approach to obtain the numerical results. More exactly, we consider, as in [19], a nonuniform grid to a better capture of the phenomena near the boundaries. The novelty consists in the fact that, in contrast with [18], we provide numerical solutions for large values of Rayleigh number.

The rest of the paper is structured as follows. The basic equations and preliminary materials are presented in Section 2. In Section 3 we describe the numerical algorithm and give some test results. Finally, in Section 4 we provide and discuss our principal results in the form of tables and figures.

2. Basic equations

A porous medium is a material consisting of a solid matrix with a interconnected void saturated by a fluid. A bidisperse porous medium, as it is mentioned in [16] or [17], is composed of clusters of large particles that are agglomerations of small particles. Examples of BDPM are beds of porous and fractured rocks, coal deposits or bidisperse catalysts. There exists a wide range of applications in geophysics, medicine or food industry, see [10], [14], [22] or [20]. Fluid flow and heat transfer in BDPM were studied for various configurations as vertical and wavy plates, channels or cylindrical geometries. The problem of steady Darcy free convection in an enclosure was analyzed in [18]. More exactly, the geometry of the model consists in a square cavity with a given size filled with BDPM, see Figure 1a. The horizontal walls are adiabatic whereas the vertical walls are kept at constant but different temperatures. The physical problem is represented mathematically by the following set of partial differential equations introduced in [18] along with the corresponding boundary conditions illustrated in Figure 1a

$$\frac{\partial u_f}{\partial x} + \frac{\partial v_f}{\partial y} = 0, \tag{2.1}$$

$$\frac{\partial u_p}{\partial x} + \frac{\partial v_p}{\partial y} = 0, \tag{2.2}$$

$$\frac{\partial p}{\partial x} = -\frac{\mu}{K_f} u_f - \xi(u_f - u_p), \tag{2.3}$$

$$\frac{\partial p}{\partial x} = -\frac{\mu}{K_p} u_p - \xi(u_p - u_f), \tag{2.4}$$

$$\frac{\partial p}{\partial y} = -\frac{\mu}{K_f} v_f - \xi(v_f - v_p) + \rho g \hat{\beta}(T_F - T_0), \tag{2.5}$$

$$\frac{\partial p}{\partial y} = -\frac{\mu}{K_p} v_p - \xi(v_p - v_f) + \rho g \hat{\beta}(T_F - T_0), \tag{2.6}$$

$$\phi(\rho c)_f \left(u_f \frac{\partial T_f}{\partial x} + v_f \frac{\partial T_f}{\partial y} \right) = \phi k_f \nabla^2 T_f + h(T_p - T_f), \tag{2.7}$$

$$(1-\phi)(\rho c)_p \left(u_p \frac{\partial T_p}{\partial x} + v_p \frac{\partial T_p}{\partial y} \right) = (1-\phi) k_p \nabla^2 T_p + h(T_f - T_p), \tag{2.8}$$

where

$$T_F = \frac{\phi T_f + (1-\phi)\varepsilon T_p}{\phi + (1-\varepsilon)\phi}, \quad T_0 = \frac{T_h + T_c}{2}.$$

Here the subscripts f and p are related to the macrophase and to the microphase, respectively. Moreover, (x, y) represent the Cartesian coordinates, (u, v) are the filtration velocity components, T is the temperature, p is the pressure, K is the permeability, g is the magnitude of the acceleration due to gravity, c is the specific heat at constant pressure, h is the inter-phase heat transfer coefficient, ϕ is the volume fraction of the f-phase, μ is the dynamic viscosity, ρ is the fluid density, ξ is the coefficient for momentum transfer between the two phases, ε is the porosity within the p-phase and $\hat{\beta}$ is the volumetric thermal expansion. In order to obtain a dimensionless form of (2.1)-(2.8) the following variables are considered

$$p = \frac{\mu k_f}{(\rho c)_f K_f} P, (u_f, v_f) = \frac{\phi k_f}{(\rho c)_f L}(U_f, V_f), (u_p, v_p) = \frac{(1-\phi)k_p}{(\rho c)_p L}(U_p, V_p)$$

$$(x, y) = L(X, Y), T_f = (T_h - T_c)\theta_f + T_0, T_p = (T_h - T_c)\theta_p + T_0.$$

The previous dimensionless variables are substituted in (2.1)-(2.8). Proceeding as in [18], we introduce the stream functions ψ_f and ψ_p given by

$$(U_f, U_p) = \frac{\partial}{\partial Y}(\psi_f, \psi_p), \ (V_f, V_p) = -\frac{\partial}{\partial X}(\psi_f, \psi_p)$$

and eliminate the pressure P. The governing equations for continuity, momentum and energy are transformed in the following dimensionless nonlinear system

$$-(1+\sigma_f)\nabla^2 \psi_f + \beta \sigma_f \nabla^2 \psi_p = Ra \left(\tau \frac{\partial \theta_f}{\partial X} + (1-\tau)\frac{\partial \theta_p}{\partial X} \right) \tag{2.9}$$

$$\sigma_f \nabla^2 \psi_f - \beta \left(\sigma_f + \frac{1}{K_r} \right) \nabla^2 \psi_p = Ra \left(\tau \frac{\partial \theta_f}{\partial X} + (1-\tau)\frac{\partial \theta_p}{\partial X} \right) \tag{2.10}$$

$$\nabla^2 \theta_f = \phi \left(\frac{\partial \psi_f}{\partial Y}\frac{\partial \theta_f}{\partial X} - \frac{\partial \psi_f}{\partial X}\frac{\partial \theta_f}{\partial Y} \right) + H(\theta_f - \theta_p) \tag{2.11}$$

$$\nabla^2 \theta_p = (1-\phi) \left(\frac{\partial \psi_p}{\partial Y}\frac{\partial \theta_p}{\partial X} - \frac{\partial \psi_p}{\partial X}\frac{\partial \theta_p}{\partial Y} \right) + H\gamma(\theta_p - \theta_f), \tag{2.12}$$

where Ra denotes the Rayleigh number, σ_f represents the inter-phase momentum transfer parameter, K_r is the permeability ratio, H is the inter-phase heat transfer parameter, γ is the modified thermal conductivity ratio, β denotes the modified thermal diffusivity ratio and τ incorporates the porosity of micropores and are defined as

follows

$$Ra = \frac{\rho g \hat{\beta}(T_h - T_c) K_f L (\rho c)_f}{\phi \mu k_f},\ \sigma_f = \frac{\xi K_f}{\mu},\ \beta = \frac{(1-\phi) k_p (\rho c)_f}{\phi k_f (\rho c)_p}$$

$$K_r = \frac{K_p}{K_f},\ H = \frac{hL^2}{\phi k_f},\ \gamma = \frac{\phi k_f}{(1-\phi)k_p},\ \tau = \frac{\phi}{\phi + (1-\phi)\varepsilon}.$$

More details about their significance and their values can be found in [8]. The independent variables (X, Y) belong to $[0,1] \times [0,1]$ and the corresponding boundary conditions are given by

$$\begin{cases} \psi_f = \psi_p = 0,\ \theta_f = \theta_p = \frac{1}{2} \text{ at } X = 0 \\ \psi_f = \psi_p = 0,\ \theta_f = \theta_p = -\frac{1}{2} \text{ at } X = 1 \\ \psi_f = \psi_p = \frac{\partial \theta_f}{\partial Y} = \frac{\partial \theta_p}{\partial Y} = 0 \text{ at } Y \in \{0,1\}. \end{cases} \tag{2.13}$$

In the rest of the paper we use the following values, considered in [16] or [17], $\phi = 0.5$, $\tau = 0.625$, $H \in \{10^{-2}, 10^2\}$, $K_r \in \{10^{-3}, 10^{-1}\}$, $\sigma_f \in \{10^{-1}, 1\}$, $Ra \in \{10^2, 10^3, 10^4\}$, $\beta \in \{1, 10\}$ and $\gamma \in \{10^{-2}, 1, 10^2\}$.

In addition, physical quantities of interest are the mean Nusselt numbers at the heated wall, given in the following dimensionless form

$$Nu_f = -\int_0^1 \left(\frac{\partial \theta_f}{\partial X}\right)_{X=0} dY, \quad Nu_p = -\int_0^1 \left(\frac{\partial \theta_p}{\partial X}\right)_{X=0} dY. \tag{2.14}$$

Moreover, an overall Nusselt number can be obtained

$$Nu_{all} = \frac{\gamma}{1+\gamma} Nu_f + \frac{\gamma}{1+\gamma} Nu_p. \tag{2.15}$$

3. Numerical algorithm

A central-finite difference scheme was used in [18] to obtain the numerical solutions of equations (2.9)-(2.12) subject to boundary conditions (2.13). Moreover, the nonlinear system of discretized equations was solved using a Gauss-Seidel iteration technique. The following convergence criterion was used to check the convergence of the method

$$\|\lambda_{new} - \lambda_{old}\| / \|\lambda_{new}\| \leq \delta, \tag{3.1}$$

where δ is a prescribed error, λ represents the unknowns ψ or θ and $\|\cdot\|$ is a given norm.

As we mentioned in Section 1, we change the algorithm proposed in [18]. More exactly, we consider a variable grid near the walls to determine the numerical solutions. The step size varies as a quadratic function. In order to illustrate the grid structure, we represent in Figure 1b the mesh of size 28×28. The smallest step size is near the boundaries, while the largest step size is in the middle of the domain. To define this grid we consider the variable grid layer thickness (v.g.l.t.), b, and the number of nodes in v.g.l.t., n_b. This allows us to compute the first step in v.g.l.t., h_b, and the total number of nodes in one direction, n. For all results presented in this paper, choosing

$\delta = 10^{-9}$ in (3.1) proves to be sufficiently small such that any smaller value produces similar results. The numerical experiments were performed on the computer cluster Kotys (see [4]).

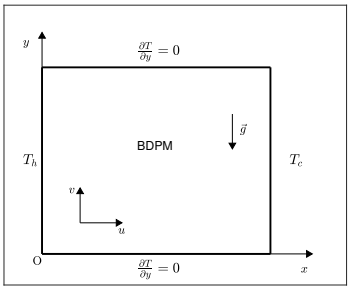

(A) The physical model

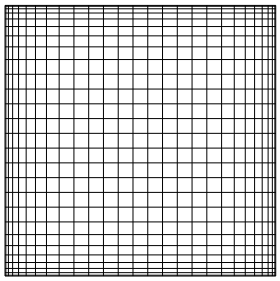

(B) The mesh with the size 28×28

In the rest of this section we provide some results related to the grid pattern and the validation of the algorithm. To determine the grid structure, we performed numerical simulations for various values of v.g.l.t., b, and different number of nodes in v.g.l.t., n_b. However, in order to save the space we restrict to present only the results from Table 1. This analysis help us to conclude that the suitable grid for the cases $Ra = 10^2$ or $Ra = 10^3$ can be based on 102×102 points, *i.e.* $b = 0.2$ and $n_b = 30$. Moreover, for the case $Ra = 10^4$ all the results are obtained using 119×119 points, *i.e.* $b = 0.2$ and $n_b = 35$.

TABLE 1. Results for different grids at $Ra = 10^4$ when $\sigma_f = 1, K_r = 10^{-1}, \beta = 1, H = 10^{-2}, \gamma = 10^{-2}$

b	n_b	h_b	n	Nu_f	Nu_p	$\max \lvert\psi_f\rvert$	$\max \lvert\psi_p\rvert$
0.2	35	0.00017	119	24.946	9.073	91.586	22.896
0.2	40	0.00013	137	24.956	9.078	91.618	22.904
0.3	40	0.00019	104	24.930	9.069	91.571	22.892
0.3	45	0.00015	117	24.947	9.074	91.603	22.900
0.4	45	0.00020	99	24.926	9.068	91.567	22.891
0.4	50	0.00016	110	24.942	9.073	91.597	22.899

Finally, Table 2 contains a comparison between the computed values of Nusselt number with the results from the open literature for different values of Rayleigh number. As it can be seen, the obtained results show a good agreement with the results reported by the mentioned authors. Therefore, we are confident that the results reported in the present paper are accurate.

At the end of this section, we mention that more details about numerical methods for partial differential equations can be found in [7] or [21]. Moreover, numerical results

TABLE 2. Comparison of Nusselt number for $\phi = \tau = \beta = 1$, $K_r = 10^{-4}$ and $\sigma_f = H = \gamma = 0$

Authors	Ra			
	10	10^2	10^3	10^4
[1]	1.079	3.160	14.060	48.330
[2]	–	3.113	–	48.900
[3]	–	4.200	15.800	50.800
[9]	–	3.141	13.448	42.583
[11]	–	3.118	13.637	48.117
[13]	1.065	2.801	–	–
[18]	–	–	13.664	–
[19]	1.078	3.108	13.613	48.208
[23]	–	3.097	12.960	51.000
Present	1.079	3.108	13.603	48.370

based on spline functions for the problem of natural convection in a square cavity filled with a fluid-saturated porous medium are provided in [12].

4. Results and discussion

In this section we present numerical results for the streamlines, isotherms and mean Nusselt numbers for the values of the parameters introduced in Section 2. More exactly, we consider constant some parameters and check the effect of the other ones. Tacking into account the fact that numerical results for $Ra \in \{10^2, 10^3\}$ were analyzed in [18], we restrict our attention to the case $Ra = 10^4$. Concerning the parameters which describe the porosities all results are given for the following values $\phi = 0.5$ and $\tau = 0.625$. Table 3 contains the values of the mean Nusselt numbers Nu_f and Nu_p defined in (2.14) and Table 4 provides the maximum absolute value of stream functions. Figs. 2–6 show the streamlines and their maximum absolute value (up) and isotherms (bottom) for $Ra = 10^4$, whereas Figs. 7–8 depict results for $Ra \in \{10^2, 10^3, 10^4\}$.

We analyze these results in the following. First of all, we can observe that for all values of governing parameters when $Ra = 10^4$ the flow is unicellular. Moreover, the results given in Table 4 show that the flow in p-phase is much slower than the flow in f-phase. From the position of isotherms in f-phase, which are not parallel with the vertical walls, we conclude that there exists a predominant convective heat transfer in macropahse.

For small values of H and γ, *i.e.* an intense thermal non-equilibrium effect is considered, the isotherms in p-phase are almost parallel with the vertical walls of the cavity, see Figure 2 or Figure 8. We deduce that in this case the heat transfer is mainly conductive in microphase. The difference between the streamlines for the two phases seems to be negligible, see Figure 2 or Figure 7. However, there exists an important difference between maximum absolute values of stream functions. For

large values of H and γ (thermal equilibrium) we observe an increasing in p-phase of convection effect, see the isotherms in Figs. 3–4. Moreover, for $H = \gamma = 10^2$ the isotherms have a very similar form, see Figure 6, the two phases being in thermal equilibrium. In addition, we observe that a thermal boundary layer near the vertical boundaries is presented. The flow in both phases is stratified and the dimension of central cells increases with the increase of H and γ. Also, the position of streamlines in Figs. 3–6 shows the existence of a boundary layer type flow.

Using the results in Table 3 we deduce that the values of Nusselt numbers increase by increasing K_r from 10^{-3} to 10^{-1}. Moreover, the results provided in Table 4 show that the maximum absolute value of stream function decreases in f-phase and increases in p-phase. The same behavior can be observed comparing Figure 2 and Figure 5 and it is in agreement with the physical situation. More exactly, K_r represents the ratio of micropermeability to macropermeability and small values of it suggest that the flow and convective heat transfer are reduced in microphase.

The increase of inter-phase momentum transfer parameter σ_f from 10^{-1} to 1 implies that the maximum absolute value of stream function decreases in macrophase and increases in microphase, see Table 4 or Figs. 3–4. This behavior is not surprising since σ_f is a measure of the way in which momentum is transferred between the two phases. An analogue situation is encountered for the heat flux, see Table 3, excepting the case $H = \gamma = 10^2$ when a strong thermal equilibrium exists and the values of both Nusselt numbers decrease.

Finally, we analyze the influence of Rayleigh number, Ra, on the flow and Nusselt numbers. We observe that the Nusslet numbers and the maximum of stream functions increase with the increasing of Ra, see Table 5 or Figure 7. An identic behavior is observed for the regular case, see Table 2. As we mentioned above, for large values of Rayleigh number we have convective heat transfer in macrophase, see Figs. 2–6 and Figure 8. Moreover, the conduction dominates the heat transfer in p-phase for $Ra = 10^2$ or $Ra = 10^3$, see Figure 8. The convection effect influences the heat transfer in microphase for $Ra = 10^4$ and it is more important when H and γ increase, *i.e.* the heat transfer between the phases occurs more rapidly.

Finally, we point out that the subject of a further paper can be represented by the study of this problem in triangular cavities with curved sides. To this end, we can use interpolation procedures introduced in [5] or [6].

TABLE 3. Nusselt numbers

γ	H	K_r	σ_f	$\beta = 1$		$\beta = 10$	
				Nu_f	Nu_p	Nu_f	Nu_p
10^{-2}	10^{-2}	10^{-3}	0.1	29.374	1.002	29.397	1.000
			1	21.586	1.005	21.604	1.000
		10^{-1}	0.1	31.673	6.468	29.610	1.255
			1	24.940	9.073	23.297	1.444
	10^{2}	10^{-3}	0.1	26.639	1.082	26.493	1.077
			1	18.691	1.080	18.456	1.069
		10^{-1}	0.1	32.852	6.468	28.253	1.355
			1	25.971	9.143	22.206	1.583
10^{2}	10^{-2}	10^{-3}	0.1	29.476	1.088	29.497	1.085
			1	21.659	1.088	21.675	1.081
		10^{-1}	0.1	31.673	6.437	29.694	1.320
			1	24.940	9.046	23.351	1.498
	10^{2}	10^{-3}	0.1	32.184	18.654	32.184	18.645
			1	23.149	15.264	23.149	15.250
		10^{-1}	0.1	32.359	19.876	32.371	18.812
			1	24.885	17.754	24.918	16.127

TABLE 4. Maximum absolute value of streamlines

γ	H	K_r	σ_f	$\beta = 1$		$\beta = 10$	
				$\max \lvert\psi_f\rvert$	$\max \lvert\psi_p\rvert$	$\max \lvert\psi_f\rvert$	$\max \lvert\psi_p\rvert$
10^{-2}	10^{-2}	10^{-3}	0.1	225.31	0.27	224.38	0.02
			1	123.20	0.36	122.25	0.03
		10^{-1}	0.1	140.39	16.51	220.36	2.59
			1	91.58	22.89	134.56	3.36
	10^{2}	10^{-3}	0.1	249.03	0.29	250.48	0.03
			1	151.01	0.45	152.76	0.04
		10^{-1}	0.1	142.66	16.78	225.99	2.65
			1	96.61	24.15	143.93	3.59
10^{2}	10^{-2}	10^{-3}	0.1	219.46	0.26	218.66	0.02
			1	119.92	0.35	119.07	0.03
		10^{-1}	0.1	139.89	16.45	215.70	2.53
			1	91.43	22.85	131.99	3.29
	10^{2}	10^{-3}	0.1	97.47	0.11	97.47	0.01
			1	70.23	0.21	70.24	0.02
		10^{-1}	0.1	97.84	11.51	98.02	1.15
			1	75.23	18.80	75.55	1.88

TABLE 5. Variation of results with Ra when $\sigma_f = 1$, $K_r = 10^{-1}$, $\beta = 1$, $H = 10^{-2}$, $\gamma = 10^2$

Ra	Nu_f	Nu_p	$\max \lvert\psi_f\rvert$	$\max \lvert\psi_p\rvert$
10^2	1.485	1.049	3.80	0.95
10^3	6.464	2.085	21.45	5.36
10^4	24.940	9.046	91.43	22.85

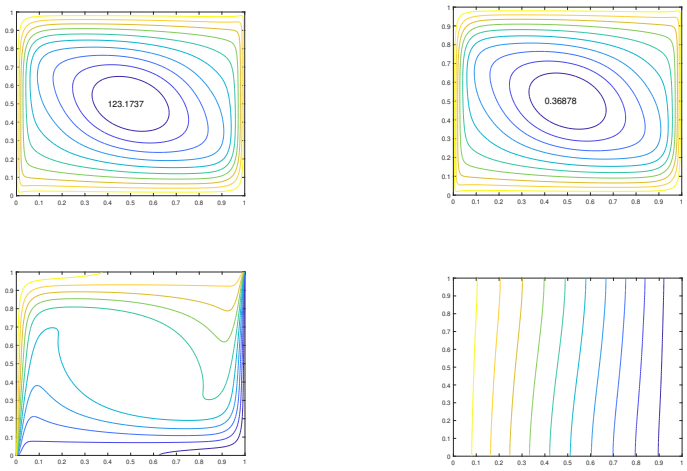

FIGURE 2. Streamlines and isotherms for $K_r = 10^{-3}$, $\sigma_f = 1$, $\beta = 1$, $H = 10^{-2}$, $\gamma = 1$: f-phase (left), p-phase (right)

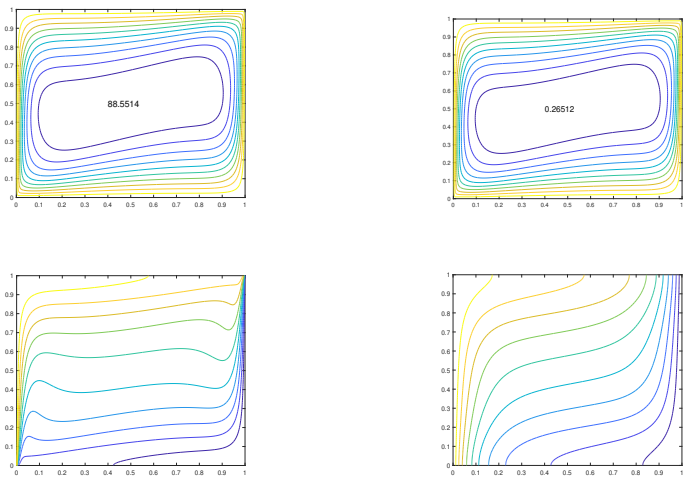

FIGURE 3. Streamlines and isotherms for $K_r = 10^{-3}$, $\sigma_f = 1$, $\beta = 1$, $H = 10^{2}$, $\gamma = 1$: f-phase (left), p-phase (right)

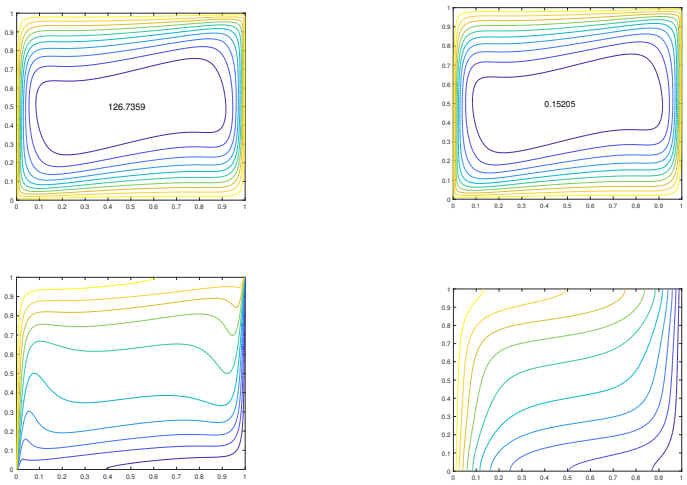

FIGURE 4. Streamlines and isotherms for $K_r = 10^{-3}$, $\sigma_f = 10^{-1}$, $\beta = 1$, $H = 10^2$, $\gamma = 1$: f-phase (left), p-phase (right)

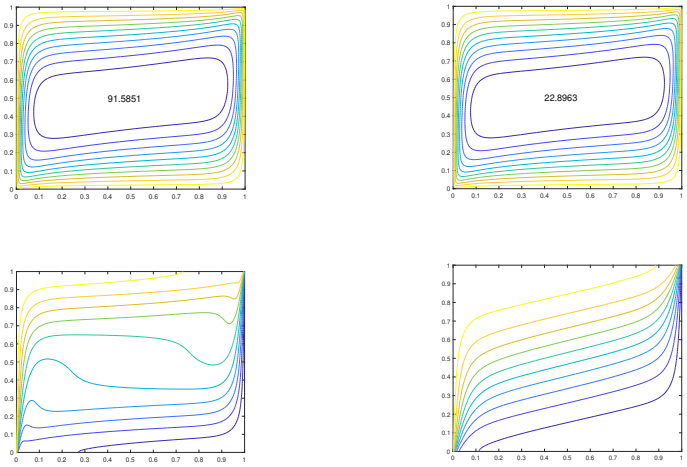

FIGURE 5. Streamlines and isotherms for $K_r = 10^{-1}$, $\sigma_f = 1$, $\beta = 1$, $H = 10^{-2}$, $\gamma = 1$: f-phase (left), p-phase (right)

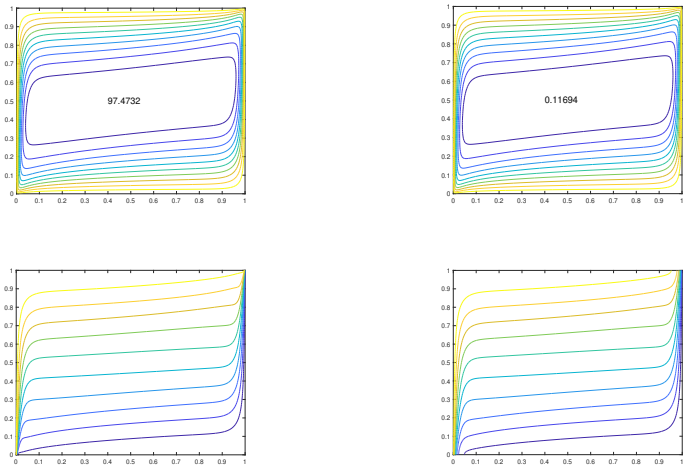

FIGURE 6. Streamlines and isotherms for $K_r = 10^{-3}$, $\sigma_f = 10^{-1}$, $\beta = 1$, $H = 10^2$, $\gamma = 10^2$: f-phase (left), p-phase (right)

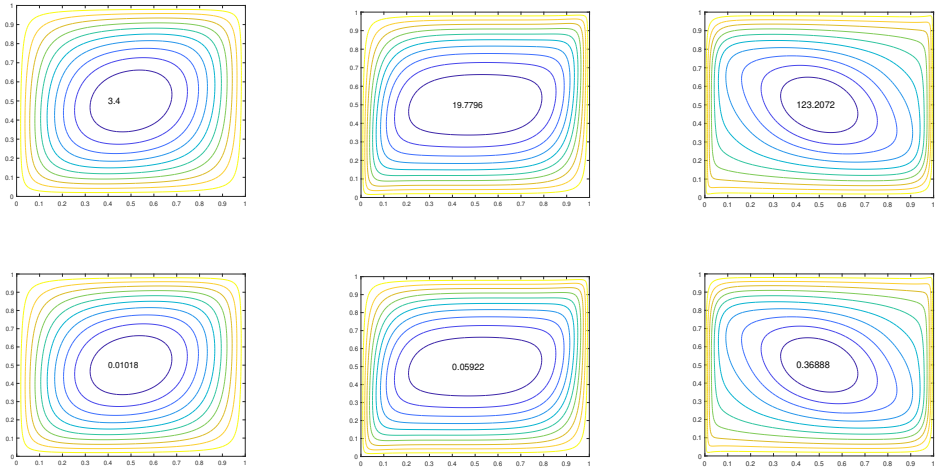

(A) $Ra = 10^3$ (B) $Ra = 10^3$ (C) $Ra = 10^4$

FIGURE 7. Streamlines for $K_r = 10^{-3}$, $\sigma_f = 1$, $\beta = 1$, $H = 10^{-2}$, $\gamma = 10^{-2}$: f-phase (up), p-phase (bottom)

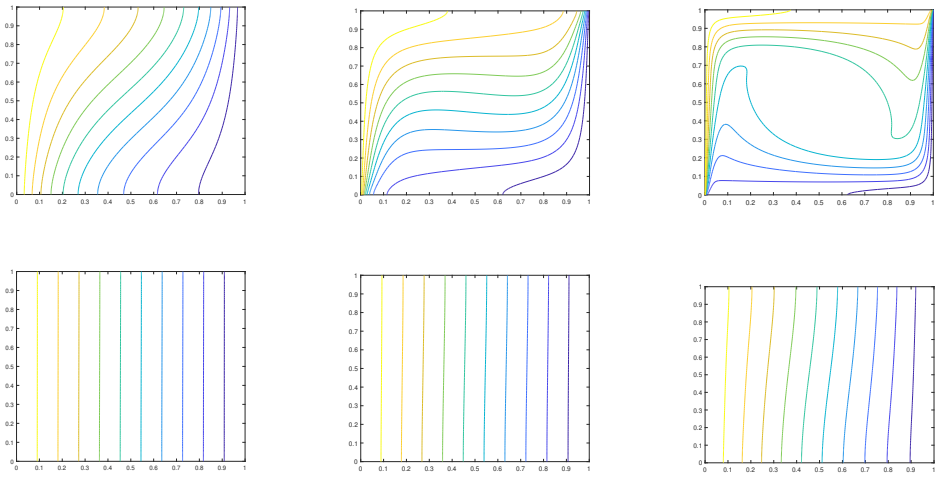

(A) $Ra = 10^2$ (B) $Ra = 10^3$ (C) $Ra = 10^4$

FIGURE 8. Isotherms for $K_r = 10^{-3}$, $\sigma_f = 1$, $\beta = 1$, $H = 10^{-2}$, $\gamma = 10^{-2}$: f-phase (up), p-phase (bottom)

References

[1] Baytas, A.C., Pop, I., *Free convection in oblique enclosures filled with a porous medium*, Int. J. Heat Mass Transf., **42** (1999), 1047-1057.

[2] Beckermann, C., Viskanta, R., Ramadhyani, S., *A numerical study on non-Darcian natural convection in a vertical enclosure filled with a porous medium*, Numer. Heat Transfer, **10** (1986), 446-469.

[3] Bejan, A., *On the boundary layer regime in a vertical enclosure filled with a porous medium*, Lett. Heat Mass Transf., **6** (1979), 93-102.

[4] Bufnea, D., Niculescu, V., Silaghi, G, Sterca, A., *Babeş-Bolyai University's high performance computing center*, Stud. Univ. Babeş-Bolyai Inform., **61**(2016), 54-69.

[5] Cătinaş, T., *Extension of some particular interpolation operators to a triangle with one curved side*, Appl. Math. Comp., **315**(2017), 286-297.

[6] Cătinaş, T., *Extension of some generalized Hermite-type interpolation operators to the triangle with one curved side*, Numer. Funct. Anal. Optim., **40**(2019), 1939-1963.

[7] Chiorean, I., Cătinaş, T., Trîmbiţaş, R., *Numerical Analysis*, Cluj University Press, Cluj-Napoca, 2010.

[8] Gentile, M., Straughan, B., *Bidispersive thermal convection with relatively large macropores*, J. Fluid Mech., **898**(2020), A14-1.

[9] Gross, R., Bear, M.R., Hickox, C.E., *The application of flux-corrected transport (FCT) to high Rayleigh number natural convection in a porous medium*, In: Proceedings of the 7th International Heat Transfer Conference, San Francisco, CA, 1986.

[10] Ingham, D.B., Pop, I. (Eds.), *Transport Phenomena in Porous Media*, vol. III, Elsevier, Oxford, 2005.

[11] Manole, D.M., Lage, J.L., *Numerical benchmark results for natural convection in a porous medium cavity*, Heat Mass Transf. Porous Media ASME Conf., **105**(1992), 44-59.

[12] Micula, S., Pop, I., *Numerical results for the classical free convection flow problem in a square porous cavity using spline functions*, Int. J. Numer. Methods Heat Fluid Flow, **31**(2021), no. 3, 753-765.

[13] Moya, S.L., Ramos, E., Sen, M., *Numerical study of natural convection in a tilted rectangular porous material*, Int. J. Heat Mass Transfer, **30**(1987), 630-645.

[14] Nield, D.A., Bejan, A., *Convection on Porous Media* (Fifth Edition), Springer, New-York, 2017.

[15] Nield, D.A., Kuznetsov, A.V., *Heat transfer in bidisperse porous media*, in: D.B. Ingham, I. Pop (Eds.), Transport in Porous Media, vol. III, Elsevier, Oxford, 2005, 34-59.

[16] Nield, D.A., Kuznetsov, A.V., *Natural convection about a vertical plate embedded in a bidisperse porous medium*, Int. J. Heat Mass Transfer, **51**(2008), 1658-1664.

[17] Rees, D.A.S., Nield, D.A., Kuznetsov, A.V., *Vertical free convective boudary-layer flow in a bidisperse porous medium*, ASME J. Heat Transfer, **130**(2008), 1-9.

[18] Revnic, C., Groşan, T., Pop, I., Ingham, D.B., *Free convection in a square cavity filled with a bidisperse porous medium*, Int. J. Therm. Sci., **48**(2009), 1826-1833.

[19] Revnic, C., Groşan, T., Pop, I., Ingham, D.B., *Magnetic field effect on the unsteady free convection flow in a square cavity filled with a porous medium with a constant heat generation*, Int. J. Heat Mass Transf., **54**(2011), no. 9-10, 1734-1742.

[20] Straughan, B., *Convection with Local Thermal Non-Equilibrium and Microfluidic Effects*, Springer, Heidelberg, 2015.

[21] Strikwerda, J.C., *Finite Difference Schemes and Partial Differential Equations* (Second Edition), SIAM, Philadelphia, 2004.

[22] Văcăraş, V., Major, Z.Z., Mureşanu, D.F., Krausz, T.L., Mărginean, I., Buzoianu, D.A., *Effect of glatiramer acetate on peripheral blood brain-derived neurotrophic factor and phosphorylated trkB levels in relapsing- remitting multiple sclerosis*, CNS & Neurological Disorders-Drug Targets, **13**(2014), 647-651.

[23] Walker, K.L., Homsy, G.M., *Convection in a porous cavity*, J. Fluid Mech., **76**(1978), 338-363.

Cornelia Revnic
University of Medicine and Pharmacy,
Faculty of Pharmacy,
8, V. Babeş Street, 400012 Cluj-Napoca, Romania
e-mail: cornelia.revnic@umfcluj.ro

Flavius Pătrulescu
Department of Mathematics,
Technical University of Cluj-Napoca,
28, Memorandumului Street, 400114 Cluj-Napoca, Romania
e-mail: Flavius.Patrulescu@math.utcluj.ro